ELSEVIER

Journal of Marine Systems 37 (2002) 47–68

JOURNAL OF MARINE SYSTEMS

www.elsevier.com/locate/jmarsys

Sharp frontal interfaces in the near-surface layer of the tropical ocean

Alexander Soloviev[a,*], Roger Lukas[b], Hiroshi Matsuura[c]

[a] *Oceanographic Center, Nova Southeastern University, 8000 North Ocean Drive, Dania Beach, FL 33004, USA*
[b] *Department of Oceanography, University of Hawaii, 1000 Pope Road, Honolulu, HI 96822, USA*
[c] *Ocean Research Department, Japan Marine Science and Technology Center, 2-15, Natsushima-cho, Yokosuka, Kanagawa, 237-0061, Japan*

Received 29 January 2001; received in revised form 30 January 2002; accepted 15 March 2002

Abstract

The small-scale structure of oceanic fronts contains important information about horizontal and vertical exchange of properties in the upper ocean. The data obtained in the western equatorial Pacific warm pool during Tropical Ocean–Global Atmosphere Coupled Ocean–Atmosphere Response Experiment (TOGA COARE) and Tropical Ocean Climate Study (TOCS) suggest that the sharp frontal interfaces occasionally observed in the upper layer of the tropical ocean may be associated with gravity currents. These gravity currents originate from the surface pools of relatively low-density (fresh and/or warm) water produced by convective rainfalls and spatially variable diurnal warming. It has been shown that frontal interfaces of less than 100 m width may interact with wind stress via the mechanism of Stommel's "overturning gate." The anisotropy of sharp frontal interfaces with respect to the wind stress direction can be predicted with a simple nonlinear model including both dissipation and dispersion effects. This study elucidates the role of fronts in the dynamics of the tropical ocean and provides important details to the description of how the temperature–salinity relationship and barrier layer in the warm pool areas are formed.

Keywords: Frontal features; Gravity induced flow; *T*/*S* diagrams; Wind stress, tropical ocean; Barrier layer

1. Introduction

Recent global surveys using the Pathfinder SST dataset reveal persistent fronts in many parts of the World Ocean (Belkin et al., 2001). Oceanic fronts have been linked to dissipation of large-scale and meso-scale horizontal inhomogeneities of the physical fields in the upper ocean (Woods, 1980; Fedorov, 1986). Although oceanic fronts are observed over a wide range of horizontal scales, turbulent mixing events in the ocean tend to occur on relatively small scales. The small-scale structure of oceanic fronts may therefore contain important information about horizontal and vertical exchange of properties in the upper ocean.

Oceanic fronts have also been linked to the process of subduction, where one water-mass sinks below ano-

* Corresponding author. Tel.: +1-954-262-3659; fax: 1-954-262-4098.
E-mail addresses: soloviev@ocean.nova.edu (A. Soloviev), rlukas@soest.hawaii.edu (R. Lukas), mat@jamstec.go.jp (H. Matsuura).

0924-7963/02/$ - see front matter © 2002 Elsevier Science B.V. All rights reserved.
PII: S0924-7963(02)00195-1

ther without substantial mixing. Subduction appears to be an important process in maintaining the salt-stratified barrier layer often found below the warm, fresh mixed layer of the western Pacific warm pool (Shinoda and Lukas, 1995; Tomczak, 1995; You, 1995; Ando and McPhaden, 1997; Vialard and Delecluse, 1998).

In the tropical oceans, convective rainfalls and associated strong solar insolation variability produce vertical and horizontal density anomalies in the upper layer of the ocean. Horizontal Coriolis forces diminish while approaching the equator, while gravity forces become more important. The puddles of relatively light (fresh or warm) water produced by rainfalls and/or diurnal warming events induce gravity currents in the near-surface layer of the ocean. The leading edge of the gravity current typically forms a sharp frontal interface (Simpson, 1987).

An important property of gravity currents is that these currents are very sensitive to any opposing or following flow in the environment (Simpson, 1987). The gravity current propagating within a weakly stratified mixed layer can generate several different modes of internal waves. The internal motions associated with these waves affect the shape of the gravity current in a resonant manner, producing a series of frontal interfaces. Depending on ambient currents (generated by surface wind stress, for example), the frontal interface may either evolve into (Soloviev and Lukas, 1997):

(a) An arrested wedge, which "freezes" the frontal structure; or
(b) A bore-like structure, which dramatically intensifies the cross-frontal exchange and leads to the elimination of the density difference across the interface.

The bore-like structure is primarily maintained by the release of a substantial part of the potential and kinetic energy of the gravity current and is therefore accompanied with substantial entrainment fluxes.

Scenario (b) is also of special interest because under conditions of variable atmospheric forcing, most of the frontal interfaces eventually get into stage (b) and rapidly evolve into a compensated state in the density field (i.e., when the cross-frontal differ-

Fig. 1. A sharp frontal line observed in the western Pacific warm pool from the R/V *Kaiyo* on 13 August 1997.

ence in temperature is compensated by that in salinity) or vanish. In the compensated front, the density ratio,

$$R = \alpha_T \Delta T / \beta_S \Delta S, \quad (1)$$

is close to 1 (here $\alpha_T = \partial \sigma_t / \partial T$ and $\beta_S = \partial \sigma_t / \partial S$ are the expansion coefficients of temperature and salinity in units kg m^{-3} $°C^{-1}$ and kg m^{-3} psu^{-1}, and the temperature and salinity differences ΔT and ΔS are taken over the frontal interface).

High-resolution horizontal measurements in the upper layer of the ocean have indicated that sharp frontal interfaces are an observable feature of the surface mixed layer of the ocean (Zenk and Katz, 1975; Soloviev and Zatsepin, 1992; Soloviev and Lukas, 1997). For example, a distinct sharp frontal line was seen on the ocean surface (Fig. 1) and recorded in the western equatorial Pacific warm pool during the Japanese Tropical Ocean Climate Study (TOCS, 1996, Cruise Report K-9709, 1997). Many sharp frontal interfaces are found in the temperature, salinity, and density records made during the Tropical Ocean–Global Atmosphere Coupled Ocean–Atmosphere Response Experiment (TOGA COARE), using bow-mounted sensors (Soloviev and Lukas, 1997; Wijesekera et al., 1999). The sharp frontal interfaces are often found in groups. Frontal interfaces of less than ~100 wide reveal anisotropy with respect to wind stress direction (Soloviev and Lukas, 1997).

In Section 2, we analyze several extreme cases of sharp fronts observed during the TOGA COARE and TOCS and, then, we consider key statistics of sharp frontal interfaces collected during TOGA COARE. The near-surface microstructure and turbulence measurements during TOGA COARE made with the bow sensors are described in detail in Soloviev et al. (1998, 1999). The large-scale context for the TOGA COARE is summarized by Lukas et al. (1995); a comprehensive overview of the results is provided by Godfrey et al. (1988). A description of the upper ocean currents, thermohaline structure, and atmospheric forcing during TOCS can be found in Matsuura (in press).

Section 3 is devoted to a proposed mechanism of coupling between the weakly stratified mixed layer and wind stress. Section 4 summarizes the results of this study.

2. Sharp frontal interfaces in the western pacific warm pool

2.1. Case studies

The western equatorial Pacific warm pool region—the TOGA COARE and TOCS domain—is characterized by heavy precipitation and generally light winds. As a result, both heat and freshwater fluxes contribute substantially to the surface buoyancy flux, and both temperature and salinity stratification is found in the upper ocean (Lukas and Lindstrom, 1991). The thermohaline fields in the warm pool area are heterogeneous and non-stationary to a surprising degree (Huyer et al., 1997). There are numerous instances of fronts in the surface layer of the ocean in the warm pool area.

Fig. 1 shows the picture of a sharp front taken from the bridge of the R/V *Kaiyo* in the western equatorial Pacific warm pool during a TOCS cruise. The sharp frontal line is roughly aligned in the east–west direction and extended from one horizon to the other. The front is clearly seen in the photograph because the wind waves to the north of the front break much more intensively than those to the south of the front. There is also some difference in ocean color across the front.

CTD stations taken along 156°E from 8°N to 3°S (prior to crossing the front) reveal a surface salinity minimum at about 5°N and a meridional salinity gradient at the equator. Fig. 2(a,c,e) demonstrates the contour plots of temperature, salinity, and σ_t density in the vicinity of the Equator (3°N–3°S). A CTD Station taken just north of the front (see map in Fig. 4) shows a nearly isothermal layer of 71 m depth (as determined from a criteria $T(1) - T(H) = 0.5$ °C) and a shallow halocline, starting from ~12 m (Fig. 2b,d). The shallow halocline is presumably related to the front. In Fig. 3, the vertical thermohaline structure of the upper 71-m layer of the ocean at this CTD station is shown in more detail. The layer between the top of the shallow halocline (the well-mixed layer) and the bottom of the nearly isothermal layer (the top of the thermocline) may be classified as the *barrier layer* (Lukas and Lindstrom, 1991). This particular case has a temperature gradient reinforcing salinity stratification. The temperature contribution, however, is approximately 2.4 times smaller than the salinity con-

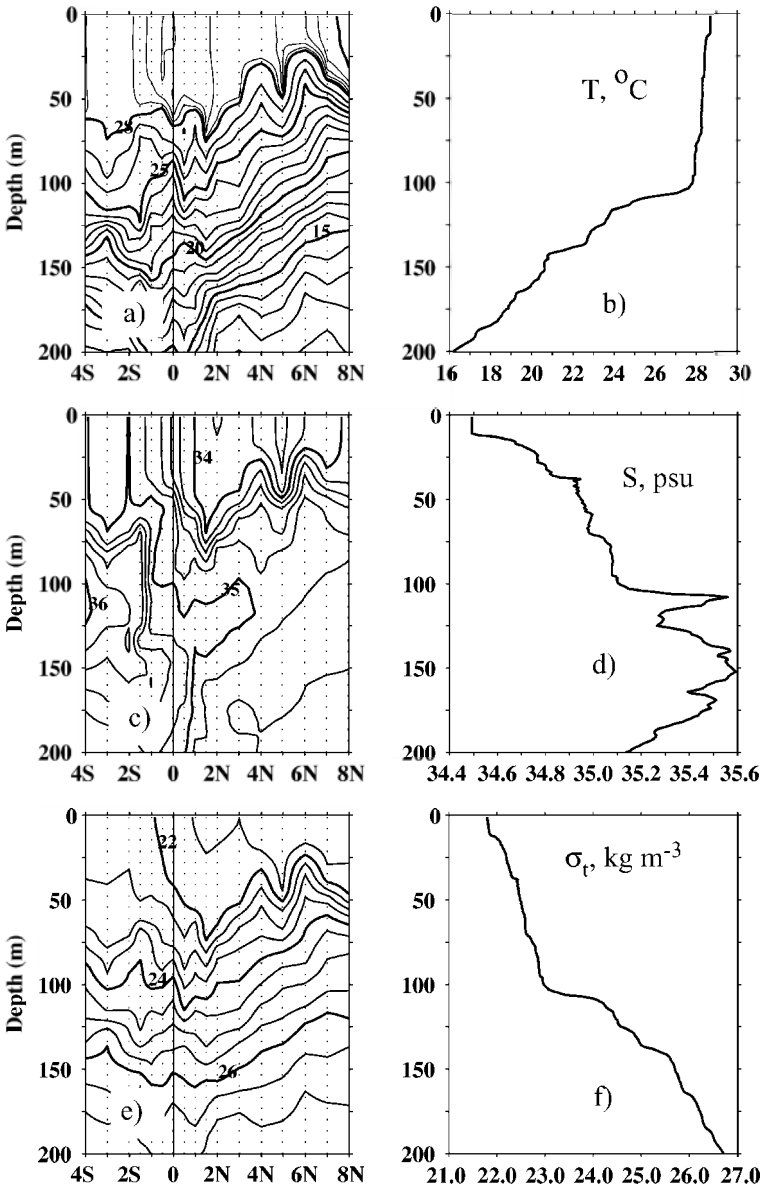

Fig. 2. Contour plots of (a) temperature, (c) salinity, and (e) density during the R/V *Kaiyo* section along 156°E. Vertical profiles of (b) temperature, (d) salinity, and (f) density calculated from the CTD station taken north of the surface front (see Fig. 4 for the position of the station relative to front). There is a 4° difference in longitude between the meridional section and the CTD station. The contour interval on plot (a) is 0.2 °C for T>28 °C and 1.0 °C for T<28 °C.

tribution into the density stratification of the barrier layer.

There is a well-mixed near-surface layer in the upper, 12 m of the ocean (Fig. 3). In a simplified two-layer model, the speed of a gravity current, U_g, developing due to the density anomaly $\Delta\rho$ is controlled by the Froude number, $F = U_g/\sqrt{g'h_0}$, where g' is the reduced gravity ($g\Delta\rho/\rho$) and h_0 is the depth of anomaly. Following Whitham (1974), we will use Favor's (cited from Whitham, 1974) critical value

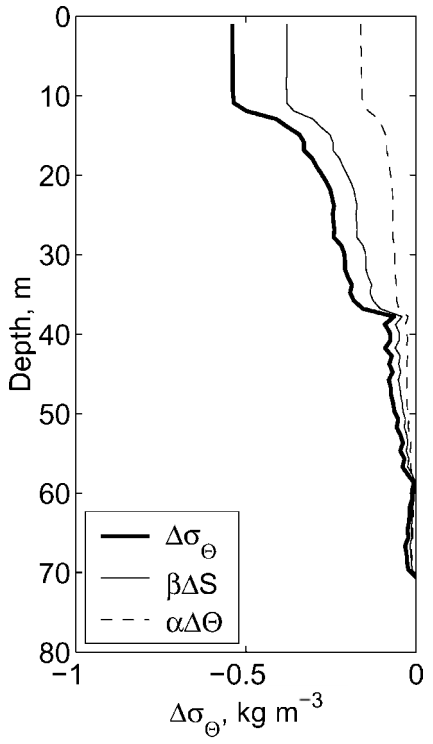

Fig. 3. Vertical distribution of potential density (σ_Θ) relative to the bottom of the mixed layer and the impact of salinity (S) and potential temperature (Θ) on stratification within the mixed layer according to the CTD Station (see also Fig. 2b,d,f). Here, α and β are the respective thermal expansion and salinity contraction coefficients; Δ is the difference operator (with respect to the bottom of the upper ocean mixed layer). The upper ocean mixed layer depth, $H = 71$ m, is determined from criteria $T(0) - T(H) = 0.5$ °C.

$F = 1.2$. Laboratory experiments described in Simpson (1987) suggest that the Froude number may depend on h_0/H. For crude estimates, we will, however, ignore this dependence. Assuming that in the example shown in Fig. 3, $h_0 = 12$ m, $H = 71$, $\Delta\rho = 0.54$ kg m^{-3}, and $F = 1.2$, the speed of gravity current due to the observed density anomaly within the mixed layer is estimated as $U_g = 0.30$ m s^{-1}. This is in fact a lower estimate since the effective thickness of the near-surface density anomaly layer driving the gravity current is larger than 12 m. The effective thickness calculated as $h_{ef} = (\rho(0) - \rho(H))^{-1} \int_0^H (\rho(z) - \rho(H))\, dz \approx 27$ m results in $U_g = 0.44$ m s^{-1}, which is an upper estimate. (Both estimates do not account for the opposing wind stress).

The ADCP record from the 16-m bin shows a jump of the relative velocity ($\Delta \boldsymbol{U} = \boldsymbol{U}_{16} - \boldsymbol{U}_{24}$) at the intersection of front of approximately 0.4 m s^{-1} (Fig. 4). This is within the range of the above estimates for the gravity current speed. (Note that the shipboard ADCP data start only from 16 m.) The contour plot of the northward velocity component during the subsequent meridional section of the R/V *Kaiyo* along 152°E (Fig. 5) reveals signatures of a strong SSE near-surface current. The sharp front visually observed in Fig. 1 can be associated with the leading edge of this near-surface current.

According to the shipboard ADCP and meteorological observations, an 8 m s^{-1} SSE wind opposed the buoyant spreading of the front (Fig. 4). (The wind speed data were taken every 3 h.) There is a jump in the horizontal velocity component normal to the front (Fig. 4). The breaking of surface waves observed north of the front (Fig. 1) can be ascribed to the effect of the surface wave–current interactions (Phillips, 1977). The modification of the surface wave field observed in Fig. 1 may also be the result of an interaction between surface waves and near-surface turbulence (Barenblatt and Benilov, 1982). Note that the propagation of the gravity current in the form of an internal bore is accompanied by generation of large-amplitude internal waves at the tail of the gravity current head (Simpson, 1987); breaking of these internal waves may generate turbulent spots in the vicinity of front.

Another observation of a sharp frontal interface is presented in Fig. 6. This is an east–west section from the R/V *Wecoma* during TOGA COARE. There are no visual observations of the ocean surface available for this section, but evidence of convergence lines were seen on sections during the preceding and following days. The data from the CTD sensor mounted on the bow of the vessel at 2 m mean depth (Wijesekera et al., 1999) provide high-resolution data in the horizontal direction, and the data from an undulating CTD (SEASOAR) provide information on the upper ocean stratification during this case study. The 3-km grid of the SEASOAR and ADCP data is, however, too sparse to resolve small-scale horizontal features. In particular, the possible internal-wave train accompanying the propagation of the gravity current cannot be resolved with a 3-km data set since its anticipated theoretical wavelength (see Section 3), $\lambda \approx 6h_0 \sim 10^2$ m.

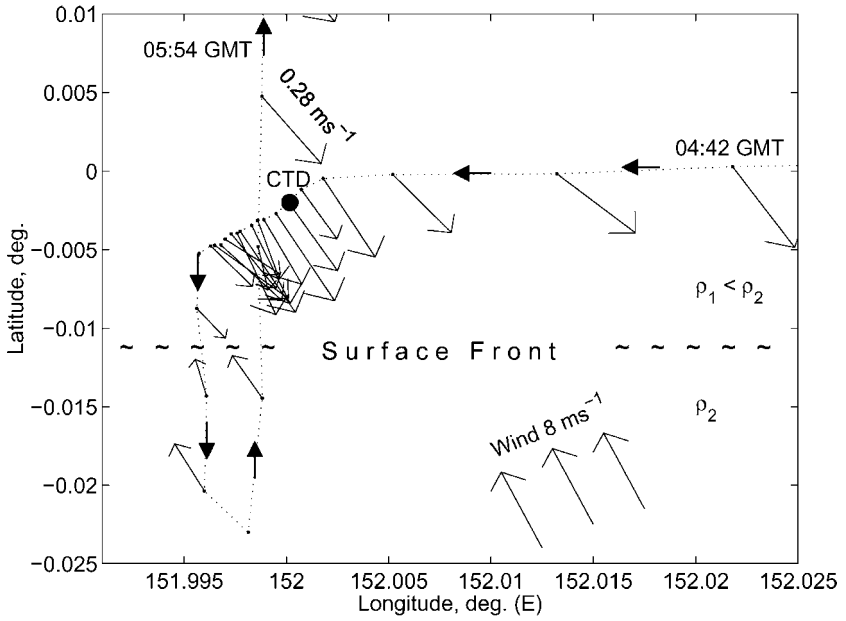

Fig. 4. Track of the R/V *Kaiyo* on 13 August 1996 (during intersection of the sharp surface front shown in Fig. 1) is given with dotted line; bold arrows heads indicate direction of ship. The time marks are on the upper right and left corners. The ADCP velocity shear vector $\Delta \boldsymbol{U} = \boldsymbol{U}_{16} - \boldsymbol{U}_{24}$ is shown along the ship track, where $\boldsymbol{U}_{16}$ and $\boldsymbol{U}_{24}$ are the horizontal velocity vectors for the 16- and 24-m bins, respectively. The scale for the velocity shear vector can be found in the upper left corner. Position of the CTD station (Figs. 2b,d,f and 3) is marked with a bold circle.

A sharp front is clearly seen in the bow record of density at 45.6 km (Fig. 6a). It is associated with a rain-formed freshwater surface lens. Note that only one boundary of this lens is sharp. The density and velocity contour plots calculated for the upper 100 m of the ocean from SEASOAR and ADCP measurements (Fig. 6b–d) reveal a density anomaly and signatures of the near-surface current associated with this frontal structure. Between 25 and 50 km (Fig. 6), the density anomaly has cyclonic vorticity (Feng et al., 2001), which appears to have been caused by the inertial spin-down of an eastward equatorial jet.

Fast-response temperature, conductivity, pressure (depth), and turbulence probes were mounted on the bow of the R/V *Moana Wave* at nominal depth of 1.7 m during COARE (Soloviev et al., 1998, 1999). Figs. 7–9 depict three examples of sharp frontal interfaces observed in the warm pool area during the R/V *Moana Wave* COARE EQ-3 cruise. In addition to high-frequency signals from the bow sensors, the corresponding records of temperature and salinity from the ship's SeaBird Electronics thermosalinograph system are also shown in Figs. 7–9.

There are increased levels of turbulence dissipation rates associated with the frontal interface in the examples in Figs. 7 and 8, while there are no signatures of turbulence variation related to the interface in the example shown in Fig. 9. In Fig. 7, the wind stress opposes the buoyant spreading of the front; the turbulence signal is substantially increased on the downwind side of the interface. In Fig. 8, the wind stress is supposedly almost tangential to the front. There is an increase in the turbulence signal associated with this frontal interface; it is, however, very localized. Note that this front is relatively weak. Fig. 9 represents a case when the wind stress has the same direction as the direction of the buoyant spreading of the front. The turbulence dissipation level does not change at the interface intersection.

These three cases represent non-compensated fronts. The differences in the turbulence signals in the vicinity of the fronts are presumably associated with the interaction of frontal interfaces with wind stress. Fig. 7 suggests that when the wind stress opposes the buoyant spreading of a sharp front, intensive cross frontal mixing may occur. It, however,

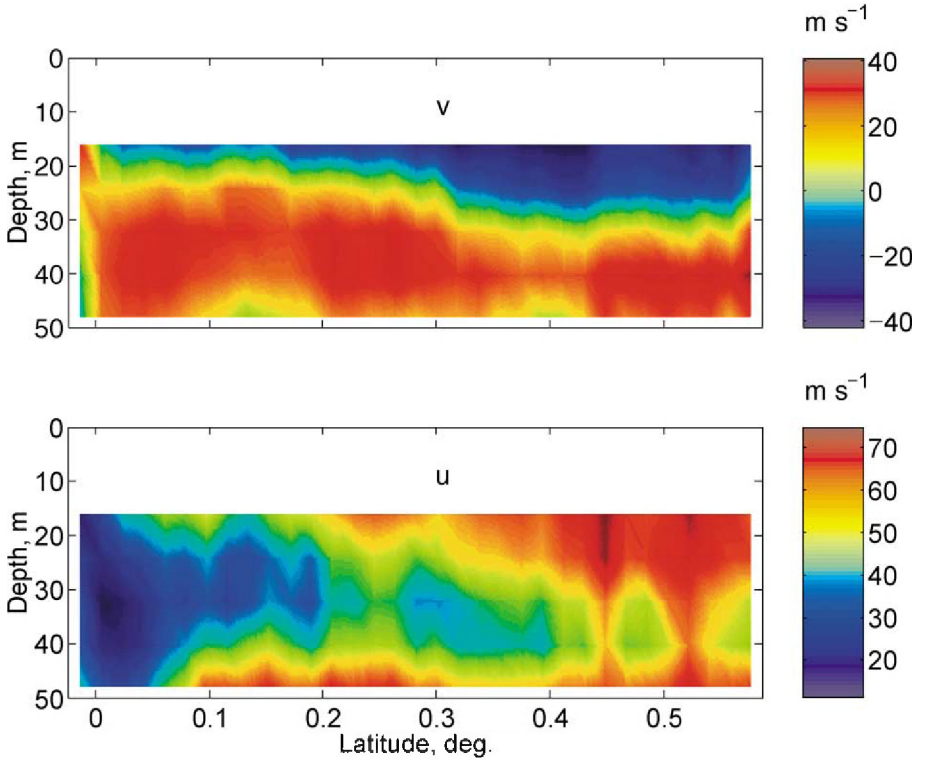

Fig. 5. ADCP velocity contour plots for north v and east u components during the meridional section of the R/V *Kaiyo* on 13 August 1996 (corresponds to the northbound part of the ship trajectory in Fig. 4 starting from 0.02°S).

should be stressed out here that in most cases, the turbulence signals cannot be confidently associated with the presence of sharp frontal interfaces. We also do not know exactly the orientation of the front with respect to the ship track or wind.

Fig. 10 demonstrates how the temperature–salinity relationship across the sharp frontal interface evolves with time when the wind stress opposes the buoyant spreading of front. During several hours the ship crossed this frontal interface back and forth several times along a snake trajectory (see Soloviev and Lukas, 1997). The interface appears to degrade considerably during several hours; the temperature–salinity relationship tends to the equilibrium state, $R = \alpha\Delta T/\beta\Delta S = 1$, which is shown by the straight diagonal line in Fig. 10. (Note that some contribution of spatial variation of the front is possible in Fig. 10.) According to the linear interpolation of the T–S tendency (Fig. 10), the compensated state of the frontal interface will be achieved at $\alpha_T\Delta T \approx 1 \times 10^{-5}$ and $\beta_S\Delta S \approx 1 \times 10^{-5}$, which corresponds to $\Delta T \approx 0.030$ °C and $\Delta S \approx 0.013$ psu.

2.2. Statistics

The case studies of sharp fronts described in the previous section represent extreme situations. In many other cases, the temperature, salinity, and density differences across fronts are relatively small. Thus, these fronts cannot be seen visually on the ocean surface as in the case shown in Fig. 1, they cannot be detected from the available ADCP measurements because they are often shallower than 16 m (Figs. 5 and 6), and they cannot be seen in the bow turbulence records as in the case shown Fig. 7. These frontal interfaces, however, can be detected in the bow density, salinity, and temperature records due to huge local gradients within the interfaces.

An algorithm for the automatic detection of sharp frontal interfaces is described in Appendix A. The

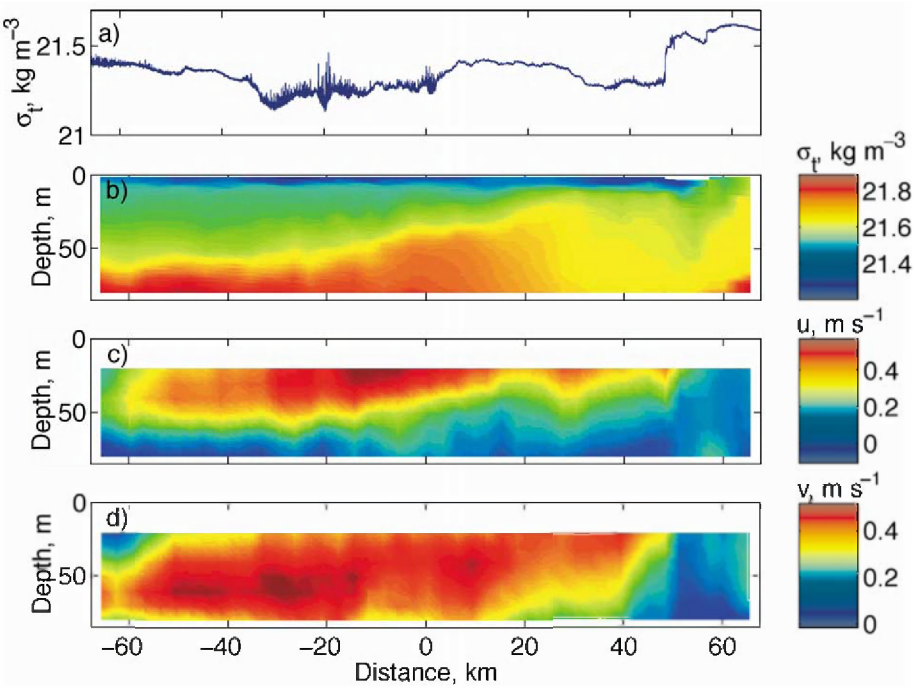

Fig. 6. (a) Sharp frontal interface in the near-surface density field measured at 2-m mean depth by a bow-mounted CTD; (b) Density contour plot calculated from a towed undulating vehicle; (c, d) Eastward and northward velocity contour plots. (6 January 1993).

ability to detect an interface depends on the ratio of the maximum gradient within the interface to the level of background fluctuations (see Eq. (A2) in Appendix A). The background fluctuation depends strongly on the environmental conditions such as wind speed, heat fluxes, presence of rain, diurnal warming and so on. An interface may be clearly seen, for example, on the salinity record but fall below the detection level in the temperature and/or density record(s). Some interfaces are therefore found simultaneously in two or three of these variables while others appear clearly in only one variable. We will call here the sharp frontal interfaces found in density, salinity, and temperature records as the *density*, *salinity*, and *temperature interfaces*, respectively.

In Fig. 11, statistical properties of the density, salinity, and temperature interfaces obtained from bow records during four TOGA COARE cruises of the R/V *Moana Wave* (MW 9301, MW 9302, MW 9410, and MW 9411) are summarized in the form of histograms. The first, second, and third rows in Fig. 11 correspond to the density, salinity, and temperature interfaces (the number of sharp fronts found in density, $N_\rho = 326$; in salinity, $N_S = 751$; and in temperature, $N_T = 412$). The statistics presented in Fig. 11 include the cross-front difference of density, salinity, and temperature (left column) and the density ratio number R for the density, salinity, and temperature interfaces expressed in terms of the Turner angle (the right column).

In the oceanographic literature, $Tu = \arctan(R)$ is known as the Turner angle (Ruddick and Turner, 1979; Kennan and Lukas, 1996). Here, we define R as in Eq. (1), which is different from that used in the literature on double diffusion but convenient for comparisons with the results of Ferrari and Rudnik (2000) obtained for horizontal processes with length scales exceeding 100 m. The Turner angle is positive when temperature and salinity tend to compensate each other in density. For compensated fronts $R = 1$ and $Tu = \pi/4$. For fronts with no temperature difference ($\Delta T = 0$), $R = 0$ and $Tu = 0$. As emphasized by Ferrari and Rudnik (2000), the advantage of using the Turner angle instead of the density ratio number is

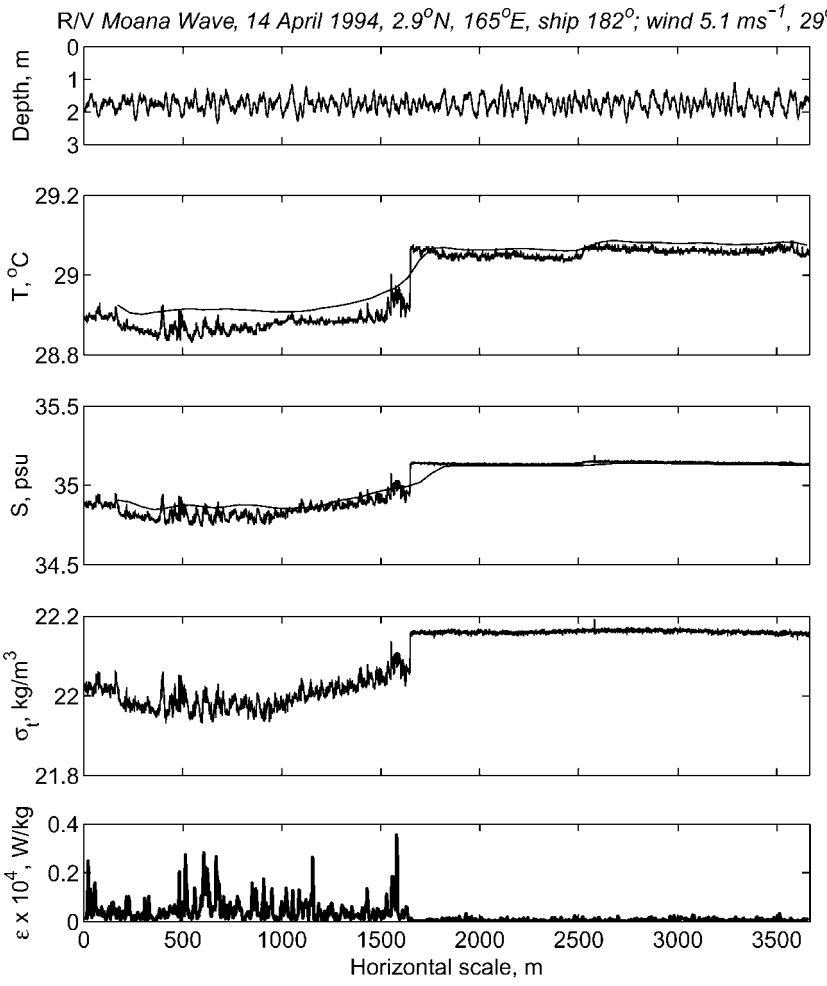

Fig. 7. The depth (pressure), temperature (T), salinity (S), density (σ_t), and the dissipation rate of the turbulent kinetic energy (ε) from bow sensors for the wind stress opposing the buoyant spreading of front. Corresponding records of temperature (bow thermistor at 3-m intake) and salinity (ship's thermosalinograph system) are shown with smooth lines.

that the infinite scale of R is replaced by a finite one running from $-\pi/2$ to $\pi/2$, and the infinite value of R at $\Delta S=0$ is well defined in terms of Tu. Also, the temperature dominated regions ($1<|R|<\infty$) and salinity-dominated regions ($0<|R|<1$) occupy the same space on the Tu scale, which in particular means that the ensemble averaging over Tu may be more accurate than that over R.

According to Fig. 11, the average density ratio number defined as $\langle R\rangle=\tan(\langle Tu\rangle)$ is relatively small for density interfaces ($\langle R\rangle=0.2$), is larger for salinity interfaces ($\langle R\rangle=0.5$), and approaches unity for temperature interfaces ($\langle R\rangle=0.9$). (The operator $\langle\rangle$ denotes ensemble averaging).

Fig. 12 shows the dependence of sharp frontal interfaces on the wind-to-ship angle, θ, (the left column) and on the wind speed, U_a, (the right column) separately for the density, salinity, and temperature interfaces (the first, second, and third rows, respectively). Salinity and temperature differences in Fig. 12c–f are multiplied by the corresponding expansion coefficients, α_T or β_S, to have comparable (density) units on all graphs. Fig. 12 represents the bow data sets collected during the four COARE cruises of

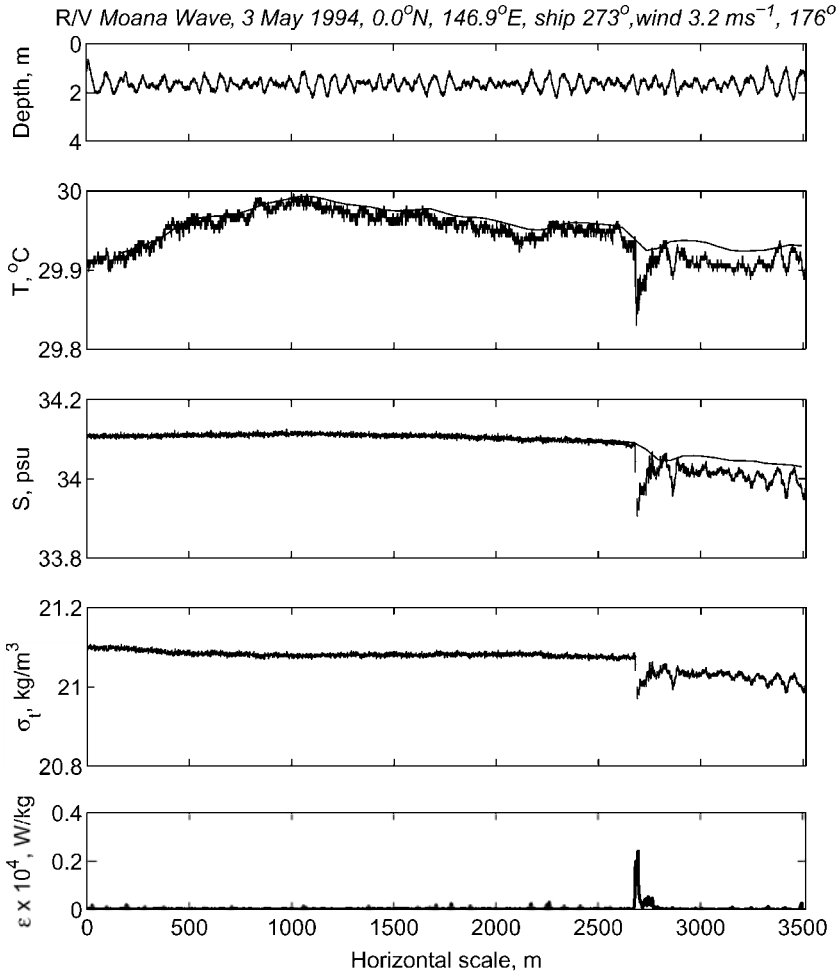

Fig. 8. Same as in Fig. 7 but for the wind stress directed along frontal line.

the R/V *Moana Wave* (same as in Fig. 11). These observations and statistics extend the results of Soloviev and Lukas (1997) to a much larger number of cases. The data in Fig. 12 are averaged on θ within $\pm 24°$ and U_a within ± 2 m s^{-1}. The vertical bars represent 1 standard error (S.E.) confidence limits calculated on the basis of Student's distribution (Rabinovich, 1995).

At the intersection of the frontal interface, we do not know exactly the intersection angle. Soloviev and Lukas (1997), nevertheless, showed that for large numbers of the frontal interfaces detected using the algorithm described in Appendix A, the average wind-to-front angle, $\langle\phi\rangle$, can be replaced with the average wind-to-ship angle, $\langle\theta\rangle$, where $\theta = \beta - \gamma$; β is the wind direction (we use the meteorological convention in this paper), and γ is the ship course. The front vector is defined here as a vector that is normal to the frontal line. The vector direction is from less to more dense water (i.e., coinciding with the direction of the buoyant spreading of the front).

According to Fig. 12, the non-compensated sharp frontal interfaces (namely, in density and salinity) appear to depend on the wind-to-front angle. The spatial anisotropy is pronounced for the density interfaces (Fig. 12a), is less pronounced (but still statistically significant) for the salinity interfaces (Fig. 12c), and is practically non-resolvable for the temperature

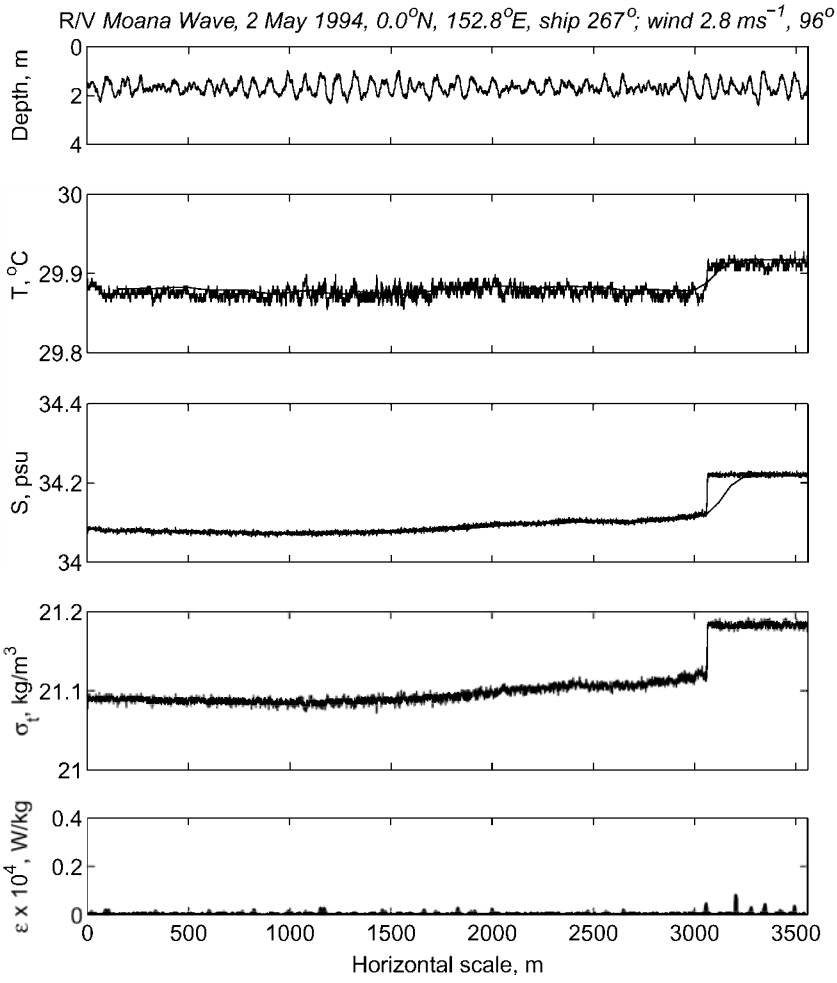

Fig. 9. Same as in Fig. 7 but for the wind stress directed from light to dense water.

interfaces (Fig. 12e). It is remarkable that the density interfaces do not seem to depend much on the wind speed magnitude (Fig. 12b), while the salinity and temperature interfaces seem to degrade with increasing wind speed. Larger error bars in Fig. 12b and f at 14 m s^{-1} average wind speed are primarily due to relatively small number of observations of the density and temperature sharp frontal interfaces under high wind speed conditions (10 and 3, respectively). For the salinity interfaces, this number is larger (37), and the confidence limits for the 14 m s^{-1} bin are smaller (Fig. 12d).

Note that according to the theory developed in the next section, the interfaces not satisfying inequality (13) cannot interact with wind stress; they are removed from the ensemble averaging in Fig. 12. Removal of this relatively small number of interfaces (see histogram in Fig. A1) results in some reduction of error bars but does not modify the main conclusions either on directional anisotropy and or on wind speed dependence of the sharp frontal interfaces.

Soloviev and Lukas (1997) who used one of the four COARE cruises of the R/V *Moana Wave* presented in this article revealed directional anisotropy of the sharp frontal density interfaces with respect to the wind stress direction. Statistics from the larger dataset analyzed in this paper have smaller confidence intervals, and are averaged over smaller angle bins ($\pm 24^\circ$

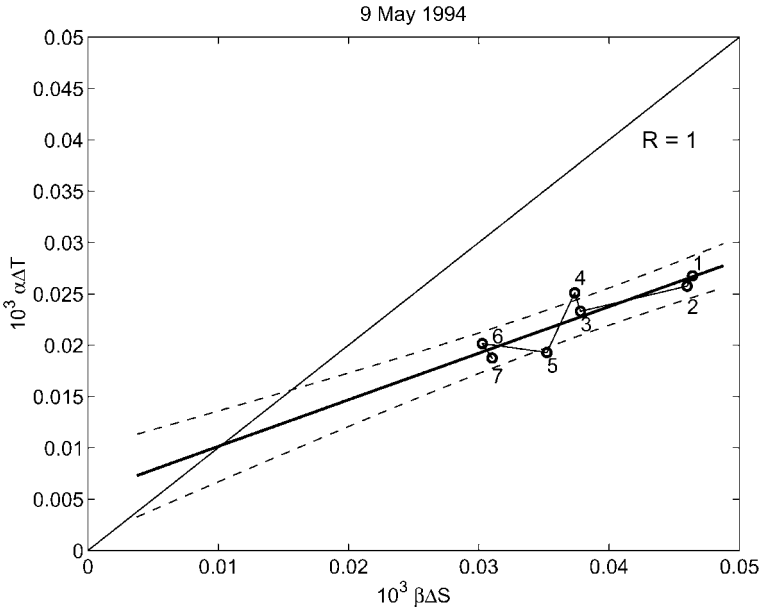

Fig. 10. Evolution of the temperature–salinity relationship during multiple intersections of a sharp frontal interfaces in the warm pool area during the R/V *Moana Wave* COARE EQ-3 cruise. The successive frontal intersections are numbered from 1 to 7 (for more details see Fig. 5 in Soloviev and Lukas, 1997). These points are linearly extrapolated (bold straight line) up to the intersection point with line $R = 1$, while the space between dashed lines contain at least 50% of the predictions.

instead of $\pm 30°$). In addition to analysis of the density interfaces, the directional anisotropy of the salinity and temperature interfaces is also analyzed here.

Soloviev and Lukas (1997) suggested that non-compensated fronts narrower than 100 m could interact with the wind stress. This mechanism is schematically shown in Fig. 13. When the wind stress is directed toward lower density, gravitational instability may trigger intensive vertical and cross-front mixing. In the process of mixing, the interface may either reach the compensated state or entirely disappear; in both cases, the interface can no longer be detected in the density field. When the wind stress is toward higher density, a vertical stratification develops which inhibits mixing. As a result, the sharp interface "freezes" and can drift with wind until the wind substantially changes its direction with respect to the front or speed. The lifetime of sharp frontal interfaces may, perhaps, be linked to the synoptic time scale for the atmospheric processes (~5 days).

This explanation is consistent with the Stommel (1993) concept of "overturning gate":

> Future observational study of the three-dimensional structures within the 'mixed' layer may show that direct driving of shear within the layer by wind overwhelms the hypothetical density-driven exchanges of thermohaline regulations. ... In the presence initially of a horizontal density gradient in the direction of the displacement, one of two events will ensue. If the displacement is toward larger mixed-layer density, then vertical stratification develops. Vertical mixing eventually occurs. There is a horizontal exchange of properties. On the other hand, if the wind-forced displacement of the surface half of the mixed layer is toward smaller density below, rapid gravitational instability will mix the two halves immediately, effectively short cutting the horizontal exchange... Therefore, there is a form of gate that opens or closes to allow horizontal flux of properties in the mixed layer, and it depends on

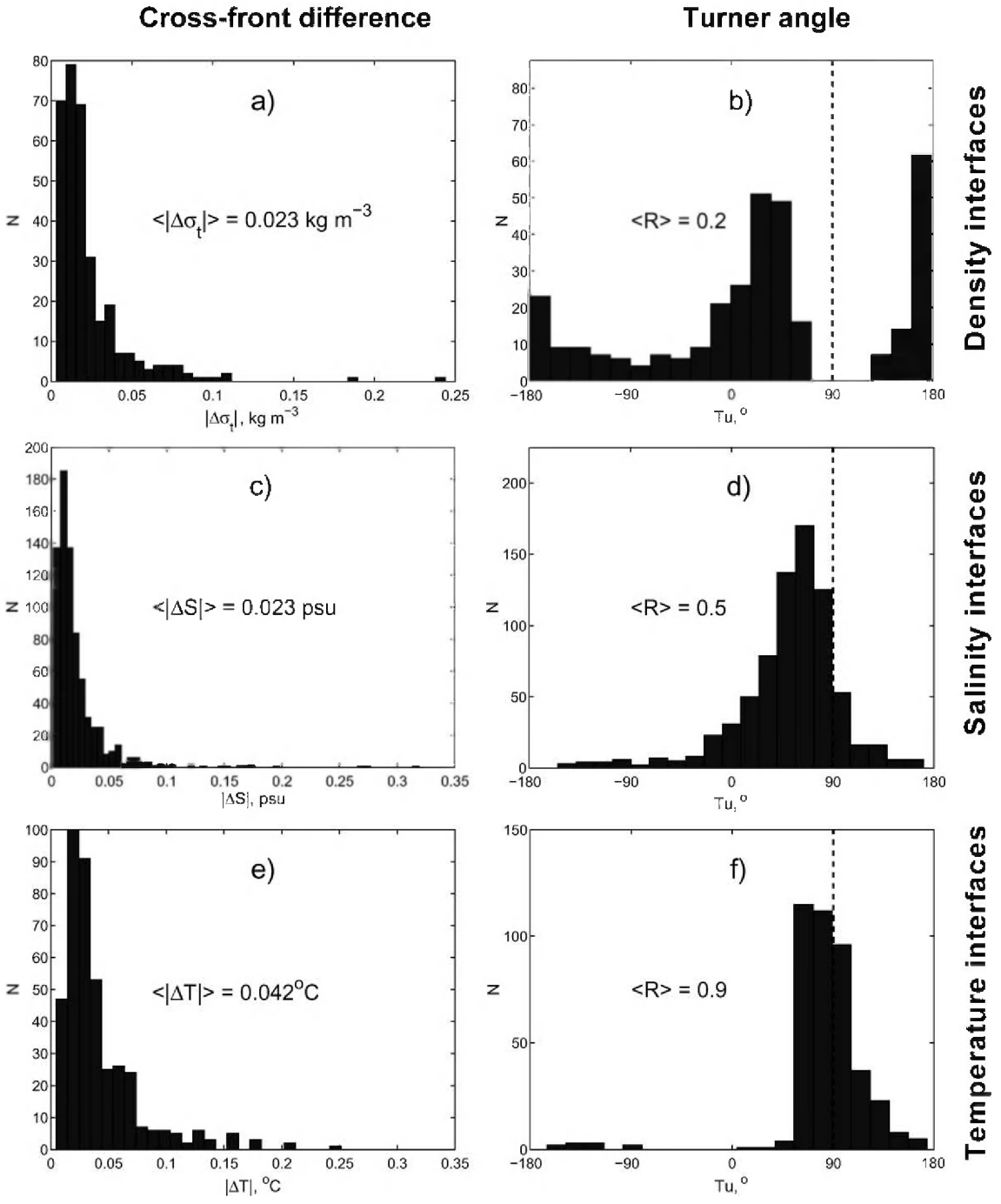

Fig. 11. Statistics of sharp frontal interfaces acquired with bow sensors during four TOGA COARE cruises of the R/V *Moana Wave* (MW 9301, MW 9302, MW 9410, MW 9411). Histograms of cross-front differences for the sharp frontal interfaces detected in (a) density, (c) salinity, and (e) temperature data and respective histograms (b, d, and f) for the Turner angle.

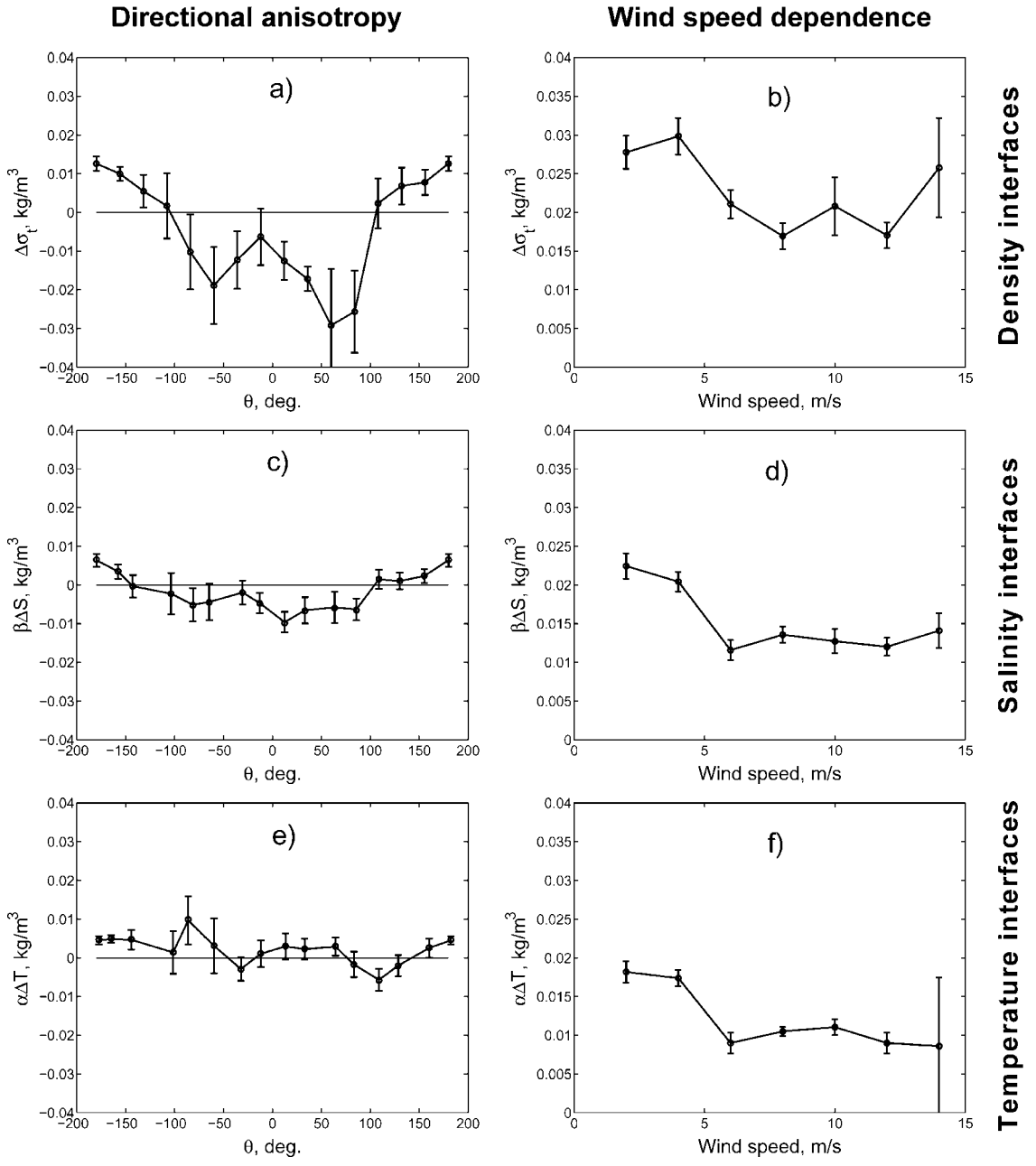

Fig. 12. Directional and wind speed dependence of the sharp frontal interfaces detected in the (a, b) density, (c, d) salinity, (e, f) temperature bow data respectively. The data are from four TOGA COARE cruises (MW 9301, MW 9302, MW 9410, and MW 9411). The temperature and salinity differences are shown as the equivalent density differences to simplify their visual comparison with the density differences on subplots a, b. The vertical bars represent 1 S.E. confidence limits calculated on the basis of Student's distribution.

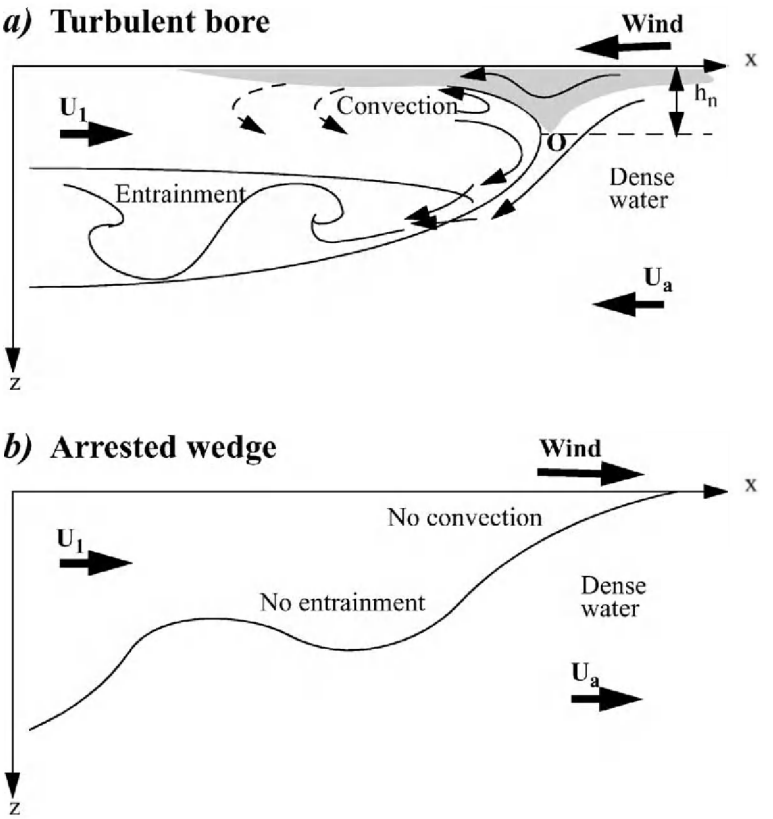

Fig. 13. Interaction of sharp frontal interface with wind stress: (a) Stommel's overturning gate is closed; (b) Stommel's overturning gate is opened.

the joint signs of displacement and local horizontal density gradient. For convenience this phenomenon may be called the *overturning gate*.

Stommel's overturning gate is open when the surface wind drift is toward higher density and closed when it is toward lower density. The spatial anisotropy of non-compensated interfaces (Fig. 12a,c) can therefore be explained by the fact that most sharp frontal interfaces are observed when the wind stress is towards higher density (the overturning gate is opened). When the wind stress is towards lower density (the overturning gate is closed) the intensive mixing effectively eliminates non-compensated sharp frontal interfaces (such an example is shown in Fig. 10). The lifetime of a non-compensated sharp frontal interface opposing the wind stress is, however, relatively small; the probability of its observation is reduced. As a result, the observed non-compensated sharp frontal interfaces demonstrate directional anisotropy with respect to the wind stress direction.

3. Interaction between wind stress and weakly stratified mixed layer

High-resolution horizontal measurements in the open ocean reveal frontal interfaces of width less than 100 m. These sharp frontal interfaces have been observed in a wide range of wind speed conditions ($0-15\ m\ s^{-1}$) and have been linked to the presence of stratification in the mixed layer. (Note that the stratification of the mixed layer is usually weak compare to the stratification of thermocline and is often found in shallow near-surface layers).

The substantial observational statistics of the sharp frontal interfaces reported in this work are from tropical latitudes only. The sharp fronts have been observed in mid-latitudes as well; these are, however, only a few case studies (Zenk and Katz, 1975; Soloviev and Zatsepin, 1992). At this point, we therefore do not know exactly how the sharp fronts are affected by the Earth's rotation. From general considerations, based on the baroclinic Rossby numbers estimates done by Soloviev and Lukas (1997), the rotation should not affect the internal structure of sharp fronts not only because of the proximity to equator (some cases are not close to the equator), but because the spatial scale is small.

Fronts are associated with larger scale anomalies; these anomalies may depend on the Earth's rotation effects (even near the equator). In particular, the sharp front observed in Fig. 6a was found at an edge of the density anomaly with cyclonic vorticity, which appears to be caused by the inertial spin-down of an eastward equatorial jet (Feng et al., 2001). In mid-latitudes, mesoscale eddies may wind the sharp fronts into spirals (Munk and Armi, 2001).

Soloviev and Lukas (1997) were able to explain some observable features of the sharp frontal interfaces in the equatorial Pacific warm pool using a "buoyant" asymptotic of the problem (neglecting rotational effects). We will use a similar theoretical approach here. This new paper, however, provides deeper insight into the problem, firstly, because of much larger observational data available and, secondly, because the theory is further developed towards the explanation of experimental facts and towards the parameterization of cross-front exchange.

The structural form of the sharp frontal interfaces has some similarity to that of the internal surge previously observed in long stably stratified lakes (Thorpe, 1971; Hunkins and Fliegel, 1973; Farmer, 1978). Evolution of an initially smooth perturbation with wavelength $L \gg h$ into an asymmetrical, shock-wave structure can be described in the framework of the shallow water theory similar to the analysis of Farmer (1978) (in our case, h is the depth of the intermediate thermocline associated with the front).

At the stage when the perturbation's slope becomes very steep, the dispersion and dissipation effects are important in this non-linear system. Whitham (1974) and Barenblatt and Shapiro (1984) applied the equation of Korteweg–deVries–Burgers type to explore a simple nonlinear system with dispersion and dissipation. In application to a two-layer upper ocean, this equation is as follows:

$$\eta_t + c_0\left(1 + \frac{3}{2}\frac{\eta}{h}\right)\eta_x + \frac{1}{6}c_0 h^2 \eta_{xxx} = \nu_e \eta_{xx}, \tag{2}$$

where η is the displacement of streamlines, t is time, x is the horizontal coordinate (in the direction of propagation), and h is the undisturbed depth of the near-surface pycnocline (for simplicity, here it is assumed that $h \ll H$, where H is the depth of the seasonal thermocline), $c_0 = (g' h)^{1/2}$ is the phase speed of disturbance, g' is the reduced gravity, and ν_e is the effective (turbulent) viscosity.

Steady propagating solutions of Eq. (2) are in the form $\eta = h\zeta(X)$, $X = x - Ut$, where U is the propagation speed of the disturbance. Integration of Eq. (2) results in (Whitham, 1974):

$$\frac{1}{6}h^2\zeta_{xx} - \frac{\nu_e}{c_0}\zeta_x + \frac{3}{4}\zeta^2 - \left(\frac{U}{c_0} - 1\right)\zeta = 0, \tag{3}$$

which can be normalized in the following way:

$$z_{\xi\xi} - m z_\xi + z^2 - z = 0, \tag{4}$$

where $\xi = [6(F-1)]^{1/2}\frac{X}{h_0}$, $z = \frac{3}{4(F-1)}\zeta$, $F = \frac{U}{c_0}$,

$$m = \left(\frac{6}{F-1}\right)^{1/2} Re_*^{-1}, \tag{5}$$

$$Re_* = h(g' h)^{1/2}\nu_e^{-1}. \tag{6}$$

Here, Re_* is the dimensionless number of Reynolds type defining the relationship between the dissipative and dispersive properties of this nonlinear system (Barenblatt and Shapiro, 1984). According to Whitham (1974), for $m < 2$, the solution is of a wave-like (soliton) type, while for $m > 2$, it is of a shock-wave (dissipative) type. The critical value of $m = 2$ at $F = 1.2$ (see Section 2) corresponds to $Re_* = Re_{cr} = 2.74$. This means that the solution of Eq. (2) is of wave-like nature (and finally evolves into a wavelike bore) for $Re_* > Re_{cr}$ and is of turbulent nature (and finally evolves into a turbulent bore) for $Re_* < Re_{cr}$.

The wavelength of the wave train that occurs at $Re_* > Re_{cr}$ can be estimated using Whitham's (1974) so-

lution of Eq. (4) as follows: $\lambda \approx 6.5[6(F-1)]^{-1/2}h_0$. At $F=1.2$ and $h_0=20$ m, this results in a 120-m wavelength.

A problem emphasized by Whitham (1974) is that the effective viscosity that can be obtained by parameterization via the mean shear flow is about 10 times smaller than necessary to achieve the critical value of Re_*. This problem, however, can be resolved by incorporating Stommel's concept of the overturning gate. When the wind stress opposes buoyant spreading of the sharp front, the convective overturning enhances the effective viscosity at the sharp frontal interface. Soloviev and Lukas (1997) parameterized the effective viscosity entering Eq. (6) as a sum of shear (ν_{shear}) and convectively (ν_{conv}) induced turbulent viscosity:

$$\nu_e \approx \nu_{\text{shear}} + \nu_{\text{conv}} = \nu_{\text{shear}} f_c, \tag{7}$$

where

$$\nu_{\text{shear}} = \kappa u_* h,\ f_c = \nu_{\text{conv}}/\nu_{\text{shear}} \approx 1 + \left[30\frac{h}{L}(\cos\phi + |\cos\phi|)\right]^{1/3} \frac{Ri_*^{1/6}}{\kappa}$$

is the factor describing convective enhancement of mixing in the frontal zone, L is the width of the frontal interface, $Ri_* = \frac{g' h}{u_*^2} = \left(\frac{c_0}{u_*}\right)^2$, c_0 is the phase speed of internal disturbances, u_* is the friction velocity in water, κ is von Karman's constant ($\kappa=0.4$), ϕ the wind direction relative to the direction of buoyant spreading of the front. At $\phi>90°$ or $\phi<-90°$, $f_c \equiv 1$, because no convective instability is possible (Stommel's overturning gate is opened); while, at $-90° < \phi < 90°$, $f_c>1$ and convective instability at the leading edge of the gravity current can develop (Stommel's overturning gate is closed).

Incorporation of parameterization (7) into (6) leads to the following relationship:

$$Re_*(Ri,\phi) \approx \frac{\kappa^{-1} Ri_*^{1/2}}{\left\{1 + [30(\cos\phi + |\cos\phi|)h/L]^{1/3} \kappa^{-1} Ri_*^{1/6}\right\}}, \tag{8}$$

which is shown in Fig. 14 (U-surface). The horizontal plane in Fig. 14 corresponds to the relationship

$$Re_* = Re_{cr} = 2.74. \tag{9}$$

For the case shown in Figs. 1–5, $Re_* \approx 2$–4; the sharp front is close to the regime of the turbulent internal bore. While, for the case shown in Fig. 6, $Re_* \approx 60$; the sharp frontal interface is far from the

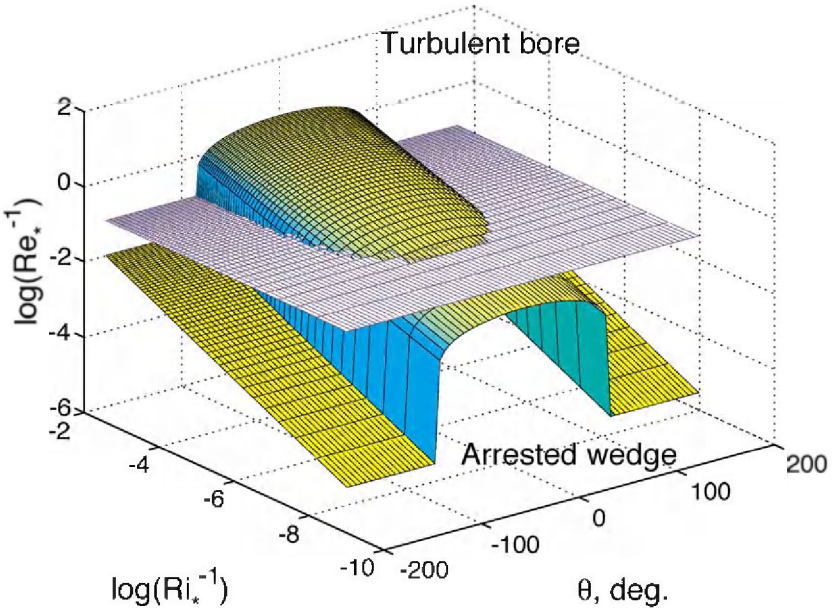

Fig. 14. Diagram for the two regimes of wind-front interaction according to Eqs. (8) and (9).

regime of turbulent bore. As we already mentioned in the previous section, the horizontal grid for the SEASOAR and ADCP data (3 km) is not sufficient to resolve the short wave internal wave trains that may accompany wave-like bores. It is speculated that from the bow data it is possible to see these short-wave oscillations at the front intersection only when the surface plume depth is relatively shallow (with respect to the sensor depth, ~ 2 m). In both cases the plume depth was much larger than 2 m.

When the wind stress direction coincides with the buoyant spreading of the front ($\theta = 180°$), Eq. (8) reduces to

$$Re_*(Ri, 180°) = \kappa^{-1} Ri_*^{1/2}. \tag{10}$$

Since $Ri_* = (c_0/u_*)^2$ and $c_0 \gg u$, the development of a turbulent bore in this situation is practically impossible. When the wind stress opposes the buoyant spreading of front ($\phi = 0°$), Eq. (8) correspondingly reduces to

$$Re_*(Ri, 0) = \frac{\kappa^{-1} Ri_*^{1/2}}{\{1 + (60h/L)^{1/3} \kappa^{-1} Ri_*^{1/6}\}}. \tag{11}$$

Estimates show that condition $Re_*(Ri_*, 0) < Re_{cr}$ (which is necessary for the development of internal turbulent bore) can be easily satisfied for weakly stratified mixed layer. For the seasonal thermocline, however, it is practically impossible to satisfy inequality $Re_*(Ri_*, 0) < Re_{cr}$ due to considerable stratification and larger depth. The response to wind forcing in the form of internal turbulent bore is therefore possible for weakly stratified mixed layers but not for the seasonal thermocline.

Since for most practical situations, $(60h/L)^{1/3} \kappa^{-1} Ri_*^{1/6} \gg 1$, formula (11) can be simplified as follows

$$Re_*(g', u_*, 0) \approx 1/60^{1/3} (g' L/u_*^2)^{1/3} = Re_L, \tag{12}$$

which contains only the parameters that are readily available from the ship underway measurements ($g' = g\Delta\rho/\rho$ is the reduced gravity, $\Delta\rho$ the density difference across the frontal interface, L the interface width, and u the frictional velocity). Re_L exceeds Re_* on the average of 7% for $h = 10$ m and of 16% for $h = 2$. (The difference between Re_L and Re_* increases with decreasing h.) Note that the algorithm described in Appendix A does not detect the sharp frontal interfaces associated with plumes of less than approximately 2-m depth, as these plumes are above the mean depth of the bow sensors.

It is remarkable that no measurement of the intermediate pycnocline depth, h, is required to calculate the *frontal Reynolds number*, Re_L, defined by formula (12). This number can therefore be estimated practically for all observations of the sharp frontal interfaces done during TOGA COARE (see Appendix A, Fig. A1). According to the theory considered here, the Stommel mechanism of the overturning gate (including the development of an internal bore) is possible in principle at

$$Re_L < Re_{cr}. \tag{13}$$

This is, however, only necessary but not sufficient condition for the internal bore regime (remember that Re_L is an asymptote of Eq. (11); the latter does not account for the wind-to-front angle dependence described with Eq. (8)).

In terms of the interface width, Eq. (13) transforms into inequality

$$L < L_{cr}, \tag{14}$$

From Eqs. (9) and (12), the critical width of the frontal interface is $L_{cr} = 1234 u_*^2/g'$. Inequality (14) means that only very sharp frontal interfaces (typically of less than 100 m width) can interact with wind stress.

Condition (13) had been applied to the data shown in Fig. 12; as a result, the error bars for the directional dependence are reduced. In fact, only 10% of the density interfaces detected from the TOGA COARE bow data using the algorithm described in Appendix A do not satisfy condition (13). According to the theory developed here these 10% of interfaces cannot interact with wind stress at any wind-to-front angle.

According to Eq. (8) (Fig. 14), the transition from the wave-like to turbulent regime occurs (if it occurs at all) almost sharply at $\phi \approx \pm 90°$. If the turbulent bore develops (wind stress is directed from dense to light water, i.e., opposes the buoyant spreading of the front), the frontal interface is intensively mixed and may disappear soon (or, perhaps, may reach a compensated state). If no turbulent bore develops (wind stress is directed from light to dense water), then the situation has some analogy to the arrested wedge

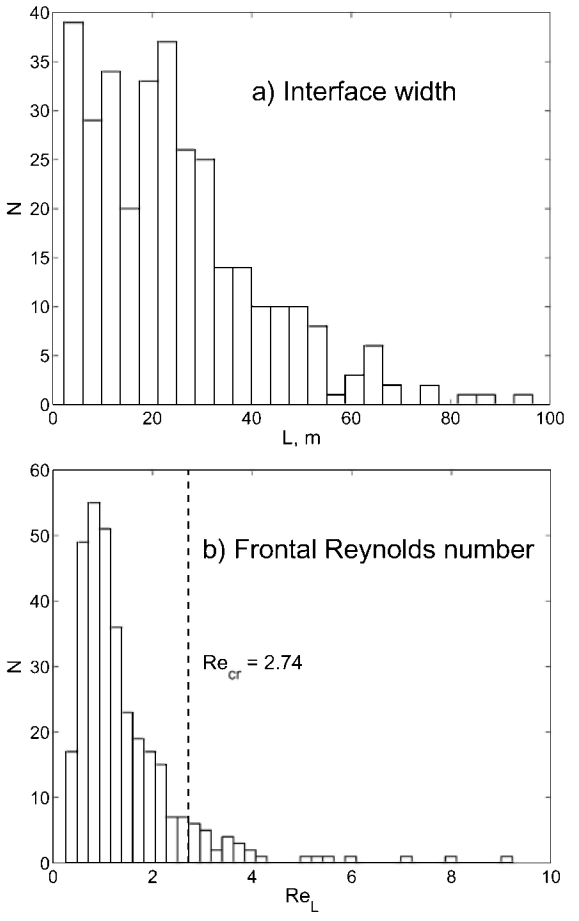

Fig. A1. Histograms of (a) width, L, and (b) frontal Reynolds number, Re_L, for the sharp frontal interfaces detected in the bow density data for four TOGA COARE cruises of the R/V *Moana Wave* (MW 9301, MW 9302, MW 9410, MW 9411).

(Simpson, 1987); the frontal interface may exist for a relatively long time, drifting with wind. This means that mainly observed are the arrested frontal interfaces, which explains the spatial anisotropy of the sharp frontal interfaces with respect to wind speed direction (Fig. 12a,c).

Due to the fact that switching from turbulent to arrested front occurs when convective overturning starts, there should be dependence on the angle rather than wind speed, which is consistent with observations (Fig. 12b). This is because convection provides more effective mixing than shear-generated turbulence. In case of compensated fronts, there is no interaction between the frontal interface and wind stress. In that case, no spatial anisotropy is expected. This is consistent with data (Fig. 12e). Some dependence on wind speed observed in Fig. 12f can be explained by the fact that the wind-induced turbulent mixing increases with wind speed, thus affecting the erosion of compensated frontal interfaces.

Thus, when the frontal interface is narrow, our results suggest that this interface may interact with wind stress. The wind stress directed towards higher density may maintain the sharp frontal interface far from its compensated state. In the opposite situation, when the wind stress is towards lower density, the enhanced cross-frontal mixing may expedite the achieving of either a compensated state or the full degradation of the frontal interface. The temperature–salinity relationship in the mixed layer of the ocean may therefore depend on the relative angle between the horizontal density gradient and the wind stress vector(!). This is a surprising conclusion, which is, however, consistent with Stommel's (1993) concept of the overturning gate.

According to Ferrari and Rudnik (2000), the horizontal density ratio R in the mixed layer is close to 1 at horizontal scales >100 m. Statistics for 1 month of observations acquired during the TOGA COARE field stage indicate that there are numerous cases of non-compensated density fronts (Fig. 11). These statistics, however, relate to the sharp interfaces only (less than ~ 100 m width) and are therefore not comparable to the results of Ferrari and Rudnik (2000).

Appearance of the sharp frontal interfaces is an indication of the subduction process. Subduction, which is an important process in forming the "barrier layer" (Lukas and Lindstrom, 1991; Shinoda and Lukas, 1995), occurs when Stommel's overturning gate is open. This happens when no turbulent bore develops, that is, when the wind is either weak or is directed along the direction of the front buoyant spreading (Fig. 13b).

In the opposite case (Sommel's overturning gate is closed), the turbulent entrainment at the sharp frontal interface may be substantial (Fig. 13a). According to Simpson (1987), the gravitational instability induced at the leading edge of a surface gravity current due to an opposing surface stress (wind stress in our case) may trigger the Kelvin–Helmholtz type instability. As the turbulent bore develops, the entrainment flux at the tail part of the gravity current head achieves relatively large value, estimated by Simpson (1987)

as being equal to approximately 0.15 times the mass flux of the gravity current itself. These considerations lead to the following parameterization of the cross-frontal mass exchange associated with the development of internal bore:

$$\langle u'\rho' \rangle = \begin{cases} c_e V_g \Delta\rho, & \text{at } Re_* \le Re_{cr} \\ \sim 0, & \text{at } Re_* > Re_{cr} \end{cases} \quad (15)$$

where u' and ρ' are deviations from the temporal or spatial mean cross-front velocity and density, $\Delta\rho$ is the density difference across the frontal interface, $c_e \approx 0.15$, V_g is the speed of the gravity current estimated here as $V_g = F(g'h)^{1/2} \approx 1.2(g'h)^{1/2}$ (see Section 2). In accordance with Eq. (8), $Re_*(Ri, \phi) \approx \kappa^{-1} \times Ri_*^{1/2}/\{1+[30(\cos\phi + |\cos\phi|)h/L]^{1/3}\kappa^{-1}Ri_*^{1/6}\}$, $Ri_* = g'h/u_*^2$, and $Re_{cr} \approx 2.74$ (see also Fig. 14). Similar formulas can be derived for the heat, salinity, and chemical substance flux by replacing in Eq. (15) the density with the temperature, salinity, or concentration, respectively.

Increased scatter of the experimental points near $\theta = -90°$ and $\theta = 90°$ in Fig. 12a possibly indicates that there are some processes that are not controlled by Stommel's overturning gate mechanism. (An alternative explanation is that the increased scatter is due to the uncertainty of the front alignment relative to the wind, which makes the sign of the cross-front component unknown when the wind is close to alignment with the front.) In particular, the tangential shear that is often observed at sharp fronts (see Figs. 4–6) may result in the formation of quasi-geostrophic eddy pairs, advection within these eddies, and the ultimate destruction of eddies with subsequent dissipation of the thermohaline structure. For mid- and high-latitudes, this mechanism can be parameterized as follows (Spall and Chapman, 1998):

$$\langle u'\rho' \rangle = c_e V_m \Delta\rho, \quad (16)$$

where V_m is a scale for the along-front velocity, $c_e \approx 0.045$ is an empirical constant. (Though constant c_e does not appear to depend on rotation effects explicitly, the validity of parameterization (16) for low latitudes has not yet been proven.)

Parameterization (16) has a structure similar to Eq. (15). The ratio of the constants, $c_b/c_e \sim 3$, and of the velocity scales, $V_g/V_m \sim 1$, suggests that the cross-front exchange due to internal bore is comparable to, perhaps exceeding, the cross-frontal exchange due to eddies.

4. Conclusions

(1) The analysis of TOGA COARE and TOCS data suggests that the sharp frontal interfaces frequently observed in the upper layer of the tropical ocean are associated with gravity currents that originate from surface pools of relatively fresh and/or warm water produced by convective rainfalls and spatially variable diurnal warming.

(2) The buoyant asymptotic of the problem (neglecting rotational effects) allows us to model some of the observed features. The appearance of sharp frontal interfaces in groups is explained by the properties of gravity currents propagating within the weakly stratified mixed layer. Frontal interfaces of width less than 100 m may interact with wind stress via the mechanism of Stommel's (1993) overturning gate. The observed anisotropy of sharp frontal interfaces with respect to the wind stress direction is described with the simple nonlinear model including both dissipation and dispersion effects. The buoyant asymptotic, however, cannot explain the considerable vorticity of the density features associated with the sharp frontal interfaces.

(3) The presence of sharp frontal interfaces is supposedly associated with the subduction process in the surface mixed layer, which is an important process in forming the barrier layer in the warm pool area. In the opposite case, when the turbulent bore develops, the associated cross-front exchange may exceed the cross-front exchange due to eddy shedding.

Acknowledgements

Anatoli Arjannikov (Granit, St. Petersburg, Russia), Jefrey Snyder and Sharon Decarlo (University of Hawaii) provided technical support to the bow measurements and the data collection aboard the R/V *Moana Wave*. Michael Gregg (University of Washington) and Robert Weisberg (University of South Florida) kindly included the bow measurements

into the program of TOGA COARE cruises MW 9301 and MW 9410 (R/V *Moana Wave*). We gratefully acknowledge the TOGA COARE collaborators Clayton Paulson, Adriana Huyer, and Michael Kosro Oregon State University), and Eric Firing and Peter Hacker (University of Hawaii) for collecting the data. The ADCP, CTD, and meteorological data from the R/V *Kaiyo* TOCS cruise were kindly provided by Y. Kashino, Yoshifumi Kuroda, and Kentaro Ando (JAMSTEC). Discussion of the first observations of sharp frontal interfaces with Grigory Barenblatt, Andrei Zatsepin, and David Farmer by one of the authors (A.S.) was important for the theoretical explanation of the observations. This study was supported with the NSF Awards OCE-9525986 and OCE-9730643.

Appendix A. Algorithm for automatic detection of sharp frontal interfaces

This algorithm developed by Soloviev and Lukas (1997) for detection of the sharp frontal interfaces in the scalar characteristic C (which is the temperature, salinity, or density) initially looks for the areas with

$$|\mathrm{d}C/\mathrm{d}x| > n\mathrm{std}(\mathrm{d}C/\mathrm{d}x), \tag{A1}$$

where $x = U_{\mathrm{ship}}t$, U_{ship} is the ship speed, t is the time and std is the standard deviation as determined from a 10-min segment. Coefficient n is an adjustable parameter. (To detect the sharpest frontal interfaces, we set $n = 4$.) To distinguish the frontal structure from the density fluctuations due to other factors, the algorithm determines the mean level of C and the standard deviation of the C fluctuations 12.5 s before and 12.5 s after the area with anomalous horizontal density gradient. The sharp frontal interface is detected if the empirical criteria

$$\Delta C > (n+1)[\mathrm{std}_1(C) + \mathrm{std}_2(C)]/2 \tag{A2}$$

is met, where $\Delta C = |C_1 - C_2|$ is the magnitude of the difference in C across the frontal interface, $C_1 = \langle C_1 \rangle_1$, $C_2 = \langle C \rangle_2$, std_1, std_2, $\langle\rangle_1$, and $\langle\rangle_2$ are the standard deviation and mean operators on 12.5-s segments correspondingly before and after the area with the anomalous gradient of C.

Characteristic $C(x)$ within the frontal interface is confined by inequality $C_1 \le C(x) \le C_2$ (if $C_1 < C_2$) or by inequality $C_1 \ge C(x) \ge C_2$ (if $C_1 > C_2$). Let x_1 and x_2 be the nearest intersection points (determined from equations $C(x_1) = C_1$ and $C(x_2) = C_2$, respectively) that contain the frontal interface in between. The width of the frontal interface is then estimated as $L = x_1 - x_2$. If two adjacent frontal interfaces overlap, they are considered to be one interface.

References

Ando, K., McPhaden, M.J., 1997. Variability of surface layer hydrography in the tropical Pacific Ocean. J. Geophys. Res. 102 (C10), 23063–23078.

Barenblatt, G.I., Benilov, A.Yu., 1982. Influence of internal waves on inhomegeneties of the ocean surface hydrophysical characteristics. The Effect of Large-Scale Internal Waves on Sea Surface, Gorkii, pp. 52–74. In Russian.

Barenblatt, G.I., Shapiro, G.I., 1984. A contribution to the theory of the wave fronts in dispersive dissipative media. Izv. Akad. Nauk SSSR, Atmos. Ocean. Phys. 20 (4), 277–284.

Belkin, I., Cornillon, P., Shan, Z., 2001. Global survey of ocean fronts from Pathfinder SST data. The Oceanography Society Biennial Scientific Meeting, 2–5 April, 2001, Miami Beach, Florida, USA. Oceanography, vol. 14(1), p. 10.

Farmer, D.M., 1978. Observations of long nonlinear internal waves in a lake. J. Phys. Oceanogr. 8 (1), 63–73.

Fedorov, K.N., 1986. The Physical Nature and Structure of Oceanic Fronts. Springer-Verlag, Berlin.

Feng, M., Lukas, R., Hacker, P., 2001. Spin-up of a sub-mesoscale eddy in the TOGA COARE Intensive Flux Array during the spin-down of an intense eastward jet. J. Phys. Oceanogr. 31 (3), 711–724.

Ferrari, R., Rudnik, D.L., 2000. Thermohaline variability in the upper ocean, COARE, November 1992 to February 1993. J. Geophys. Res. 105 (C7), 16857–16883.

Godfrey, J.S., Houze Jr., R.A., Johnson, R.H., Lukas, R., Redelsperger, J.-L., Sumi, A., Weller, R. 1988. Coupled Ocean–Atmosphere Response Experiment (COARE): an interim report. J. Geophys. Res. 103 (C7), 14395–14450.

Hunkins, K., Fliegel, M.J., 1973. Internal undular surges in Seneca Lake: natural occurrence of solitons. J. Geophys. Res. 78 (3), 539–548.

Huyer, A., Kosro, P.M., Lukas, R., Hacker, P., 1997. Upper-ocean thermohaline fields near 2S, 156N during TOGA COARE, November 1992 to February 1993. J. Geophys. Res. 102 (C6), 12749–12784.

Kennan, S.C., Lukas, R., 1996. Saline intrusions in the intermediate waters north of Oahu, Hawaii. Deep-Sea Res. 43 (2–3), 215–241.

Lukas, R., Lindstrom, E., 1991. The mixed layer of the western equatorial Pacific Ocean. J. Geophys. Res. 96 (Supplement), 3343–3358.

Lukas, R., Webster, P.J., Ji, M., Leetmaa, A., 1995. The large-scale context for the TOGA Coupled Ocean–Atmosphere Response Experiment. Meteorol. Atmos. Phys. 56, 3–16.

Matsuura, H., 2002. Observed variations of upper ocean zonal currents in the western equatorial Pacific and their relation to the local wind. J. Geophys. Res. (in press).

Munk, W., Armi, L., 2001. Spirals on the sea: a manifestation of upper-ocean stirring. From Stirring to Mixing in a Stratified Ocean, Proceedings 'Aha Huliko'a Hawaiian Winter Workshop, University of Hawaii at Manoa, January 16–19, 2001SOEST Spec. Publ., 81–86.

Phillips, O.M., 1977. The Dynamics of the Upper Ocean. Cambridge Univ. Press, Cambridge, UK.

Rabinovich, S.G., 1995. Measurement Errors: Theory and Practice. AIP Press, Woodbury, NY.

Ruddick, B.R., Turner, J.S., 1979. The vertical length scale of double-diffusive intrusions. Deep-Sea Res. 26 (8A), 903–913.

Shinoda, T., Lukas, R., 1995. Lagrangian mixed layer modelling of the western equatorial Pacific. J. Geophys. Res. 100 (C2), 2523–2541.

Simpson, J.E., 1987. Gravity Currents: In Environment and the Laboratory. Ellis Horwood, New York.

Soloviev, A., Lukas, R., 1997. Sharp frontal interfaces in the near-surface layer of the ocean in the western equatorial Pacific warm pool. J. Phys. Oceanogr. 27 (6), 999–1017.

Soloviev, A.V., Zatsepin, A.G., 1992. Response of density depression pool to wind forcing. Abstract, 24th International Liege Colloquium on Ocean Hydrodynamics: "Sub-Mesoscale Air–Sea Interaction," Liege, Belgium, May 4–8, 1992. GHER/Model Environment, pp. 99–100.

Soloviev, A., Lukas, R., DeCarlo, S., Snyder, J., Arjannikov, A., Turenko, V., Baker, M., Khlebnikov, D., 1998. A near-surface microstructure sensor system used during TOGA-COARE: Part I. Bow measurements. J. Atmos. Ocean. Technol. 15 (4), 563–578.

Soloviev, A., Lukas, R., Hacker, P., Baker, M., Schoeberlein, H., Arjannikov, A., 1999. A near-surface microstructure sensor system used during TOGA COARE: Part II. Turbulence measurements. J. Atmos. Ocean. Technol. 16 (9), 1598–1618.

Spall, M., Chapman, D., 1998. On the efficiency of baroclinic eddy heat transport across narrow fronts. J. Phys. Oceanogr. 28 (11), 2275–2287.

Stommel, H., 1993. A conjectural regulating mechanism for determining the thermohaline structure of the oceanic mixed layer. J. Phys. Oceanogr. 23 (1), 142–148.

Thorpe, S.A., 1971. Asymmetry of the internal seiche in Loch Ness. Nature 231 (5301), 306–308.

TOCS, 1996. Cruise Report K-9709. JAMSTEC, 1997, Yokosuka, Kanagawa, Japan.

Tomczak, M., 1995. Salinity variability in the surface layer of the tropical western Pacific Ocean. J. Geophys. Res. 100 (C10), 20499–20515.

Vialard, J., Delecluse, P., 1998. An OGCM study for the TOGA decade: Part II. Barrier layer formation and variability. J. Phys. Oceanogr. 28 (C6), 1089–1106.

Wijesekera, H.W., Paulson, C.A., Huyer, A., 1999. The effect of rainfall on the surface layer during a westerly burst in the western equatorial Pacific. J. Phys. Oceanogr. 29 (4), 612–632.

Whitham, G.B., 1974. Linear and Nonlinear Waves. Wiley, New York.

Woods, J.D., 1980. The generation of thermohaline fine structure of fronts in the ocean. Ocean Model. 32, 1–4.

You, Y., 1995. Salinity variability and its role in the barrier-layer formation during TOGA COARE. J. Phys. Oceanogr. 25 (11, pt. 1), 2778–2807.

Zenk, W., Katz, E.J., 1975. On the stationarity of temperature spectra at high horizontal wave numbers. J. Geophys. Res. 80 (27), 3885–3891.